

www.acsami.org Research Article

# Multiscale Manufacturing of Amorphous Alloys by a Facile Electrodeposition Approach and Their Property Dependence on the Local Atomic Order

Maryam Sadeghilaridjani, Yu Chia Yang, Vahid Hasannaeimi, Chaitanya Mahajan, Shristy Jha, Mayur Pole, Zhenhai Xia, and Sundeep Mukherjee\*



Cite This: ACS Appl. Mater. Interfaces 2021, 13, 9260-9271



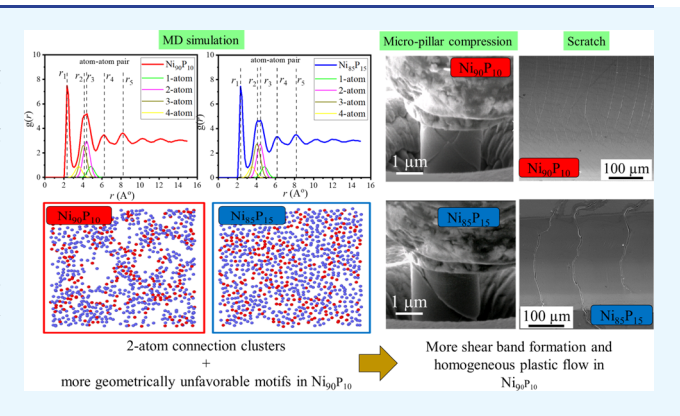
ACCESS

Metrics & More

Article Recommendations

Supporting Information

ABSTRACT: Metallic glasses are a unique class of materials combining ultrahigh strength together with plastic-like processing ability. However, the currently used melt quenching route to obtain amorphous alloys has a high cost basis in terms of manufacturing and expensive constituent elements often necessary to achieve the glassy state, thus hindering widespread adoption. In contrast, multimaterial electrodeposition offers a low-cost and versatile alternative to obtain amorphous alloys. Here, we demonstrate multiscale manufacturing of a model binary amorphous system by a facile and scalable pulsed electrodeposition approach. The structural and mechanical characteristics of electrodeposited Ni–P metallic glasses are investigated by a combination of experiments and molecular dynamics simulations. The property dependence on slight change in alloy chemistry is explained by the fraction of short-



range-order clusters and geometrically unfavorable motifs. Bicapped square antiprism polyhedra clusters with two-atom connections result in more homogeneous deformation for  $Ni_{90}P_{10}$  metallic glass, whereas a relatively higher fraction of three-atom connections in  $Ni_{85}P_{15}$  metallic glass leads to higher strength, albeit localized and relatively brittle failure. The practicality of our approach is likely to stimulate the use of amorphous alloys in simple chemistries for multiscale use with systematic property optimization for specific applications.

KEYWORDS: multiscale, manufacturing, amorphous alloys, atomic ordering, molecular dynamics simulation

## ■ INTRODUCTION

Amorphous alloys or metallic glasses have undergone tremendous development over the past six decades since first reported in 1960 for the Au-Si system. The lack of crystalline order in these materials results in a gamut of remarkable attributes including high strength and hardness, excellent wear and corrosion resistance, close to theoretical elasticity, and soft magnetic and catalytic properties.<sup>2,3</sup> In addition, amorphous alloys may be thermoplastically processed in the supercooled liquid region above their glass transition temperature and shaped into complex geometries. However, glass formation by rapid cooling of the liquid is limited by the ability to bypass crystallization. The melt-quenching route to obtain amorphous alloys and the combination of elements which allow such a processing significantly increases the cost basis for metallic glass manufacturing. In contrast, multimaterial electrodeposition for obtaining amorphous alloys offers a facile, low-cost, and versatile alternative. Both direct current (DC) and pulsed current (PC) approaches may be used for obtaining alloys with a wide range of constituent elements and desirable properties by appropriate control of electrolyte composition, temperature, pH, and deposition current density and potential. Amorphous alloys may be obtained in simple chemistries that are extremely difficult (if not impossible) to obtain by the traditional route of rapid melt quenching. However, the conditions necessary or rules for glass formation by multielement electrodeposition are not well established and there is limited understanding of property dependence on the structure and composition in electrodeposited metallic glasses (EMGs).

Here, we establish the versatility of pulsed electrodeposition as a multiscale manufacturing approach for obtaining fully amorphous bulk materials to micron-scale metallic glasses down to nanostructures of the same composition in complex

Received: December 14, 2020 Accepted: February 2, 2021 Published: February 15, 2021





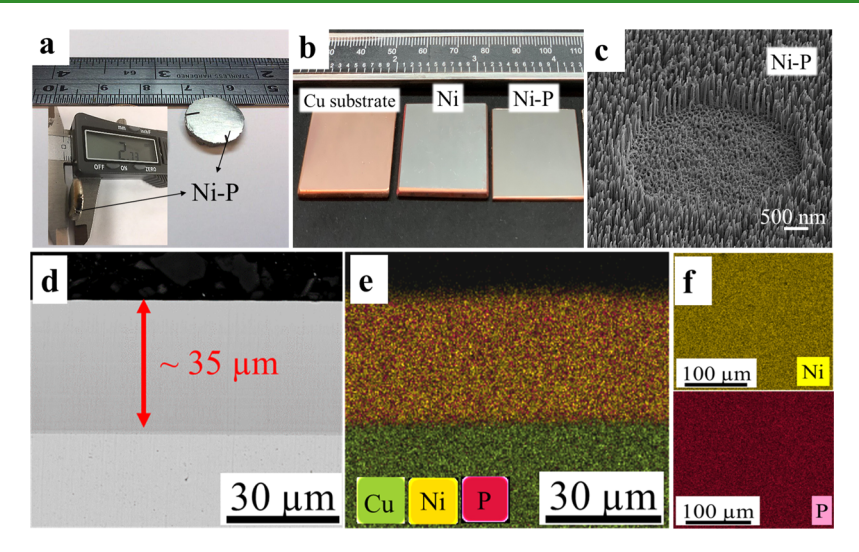


**Figure 1.** Multiscale manufacturing of amorphous alloys by a facile electrodeposition approach: (a) top view and side view (inset) of a bulk amorphous Ni–P disk with a thickness of >2.5 mm fabricated by pulsed electrodeposition; (b) micron-scale Ni–P coating synthesized through pulsed electrodeposition alongside electrodeposited Ni and the Cu substrate used; (c) free-standing Ni–P nanowires with a diameter of 80 nm synthesized through template-assisted pulsed electrodeposition; (d) cross-sectional SEM image for the Ni<sub>85</sub>P<sub>15</sub> alloy, indicating a clean and smooth surface free from pores, cracks, and other defects with a uniform thickness of ~35 μm; (e,f) cross-sectional and top-view EDS map for the Ni<sub>85</sub>P<sub>15</sub> alloy showing uniform distribution of Ni and P.

geometries. We use binary Ni-P as a model system and elucidate the change in local atomic structure and associated properties as a function of composition of the electrodeposited metallic glasses. Ni-P alloys have attracted considerable interest in the formation of coatings because of their excellent corrosion resistance<sup>6</sup> and good wear behavior<sup>7</sup> for a wide range of applications including oil and gas, microelectronics industry as diffusion barriers, aerospace, automotive, food industries, and medical instrumentation.8 A minor change in alloy chemistry may have a significant effect not only on properties but also on the atomic structure of metallic glasses in terms of short-range order (SRO) and medium-range order (MRO), 10,111 which depends on the atomic size ratio between the solute and solvent atoms and the solute concentration. Specifically, two amorphous alloys were chosen in the Ni-P system with slightly different compositions but distinctly different deformation behavior. The Ni<sub>90</sub>P<sub>10</sub> alloy showed smooth nanoindentation load-depth profiles, higher strain rate sensitivity, multiple shear band formation in micropillar compression, and ductile scratch response, all of which are characteristic of homogeneous plastic flow. This was attributed to the higher fraction of geometrically unfavorable motifs (or "liquid-like" regions) in  $Ni_{90}P_{10}$  that favor the nucleation of homogeneously distributed shear transformation zones. In contrast, Ni<sub>85</sub>P<sub>15</sub> metallic glass showed relatively more brittle behavior and localized deformation. Molecular dynamics (MD) simulations show that bicapped square antiprism polyhedra clusters with two-atom connections result in more homogeneous deformation for Ni<sub>90</sub>P<sub>10</sub>, whereas a higher fraction of three-atom connections in the Ni<sub>85</sub>P<sub>15</sub> alloy lead to localized failure.

## RESULTS AND DISCUSSION

**Multiscale Manufacturing.** The versatility of pulsed electrodeposition used in this study as a multiscale manufacturing approach is demonstrated in Figure 1. Fully amorphous Ni–P alloys were obtained in bulk dimensions with a thickness of >2.5 mm (Figure 1a) and in the form of

micron-scale coatings (Figure 1b) by limiting the deposition time. Optical microscopy images of the electrodeposited alloys in a wide range of compositions along with the underlying Cu substrate are shown in Supporting Information, Figure S1, indicating a bright and shiny surface for the as-deposited amorphous alloys. Free-standing Ni-P amorphous nanowires of identical composition as the bulk counterpart were synthesized as shown in Figure 1c, with a diameter of 80 nm. 13 Commercially available anodic aluminum oxide (AAO) nanomolds were used as templates for obtaining nanowires with different aspect ratios. Electrodeposition offers much greater flexibility in terms of direct deposition onto a templated substrate of complex geometry as opposed to the two-step process of melt quenching followed by thermoplastic forming of metallic glasses. Figure 1d shows the cross-sectional scanning electron microscopy (SEM) image of electrodeposited Ni<sub>85</sub>P<sub>15</sub>, indicating a clean and smooth surface free from pores, cracks, and other defects (coatings of other compositions had very similar characteristics). The crosssectional and top-view energy-dispersive spectroscopy (EDS) maps in Figure 1e,f, respectively, indicate homogeneous distribution of the constituent elements in the microscale coatings and the bulk alloys. The composition of the alloys was tuned by controlling the peak current density.8,12 The use of the electrodeposition approach in complex geometries and corresponding mechanical property enhancement is illustrated in Supporting Information, Figures S2 and S3. A pure copper wire coated with amorphous Ni-P showed a uniform thickness and elemental distribution (Supporting Information Figure S2), and the corresponding stress-strain curves (Supporting Information Figure S3) showed an increase in tensile yield strength from ~50 MPa for pure Cu to ~65 MPa for Ni-Pcoated Cu wire. The electrodeposited wire showed serrated flow behavior after yielding, a typical characteristic of shear band formation in amorphous alloys (Supporting Information, Figure S3b).

**Structural Characterization.** Structural characterization of the  $Ni_{100-x}P_x$  (x = 0, 5, 10, 15, and 25 at. %)

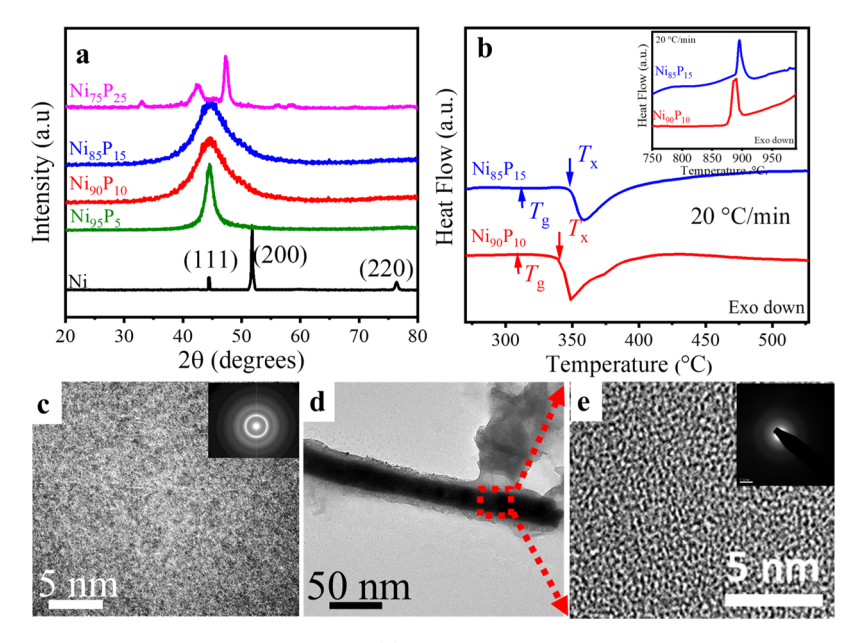


Figure 2. Structural characterization of electrodeposited alloys: (a) XRD plot for electrodeposited Ni–P alloys showing transition from the crystalline to amorphous structure; (b) DSC plot for electrodeposited amorphous  $Ni_{90}P_{10}$  and  $Ni_{85}P_{15}$  alloys at a heating rate of 20 °C/min, showing glass transition temperature ( $T_g$ ) and crystallization temperature ( $T_x$ ) with the region around the melting point shown as an inset; (c) HRTEM and inset SAED patterns for the  $Ni_{85}P_{15}$  electrodeposited alloy; (d) bright-field TEM and (e) HRTEM images of a  $Ni_{85}P_{15}$  nanowire with the inset in e showing the SAED pattern, indicating its amorphous structure.

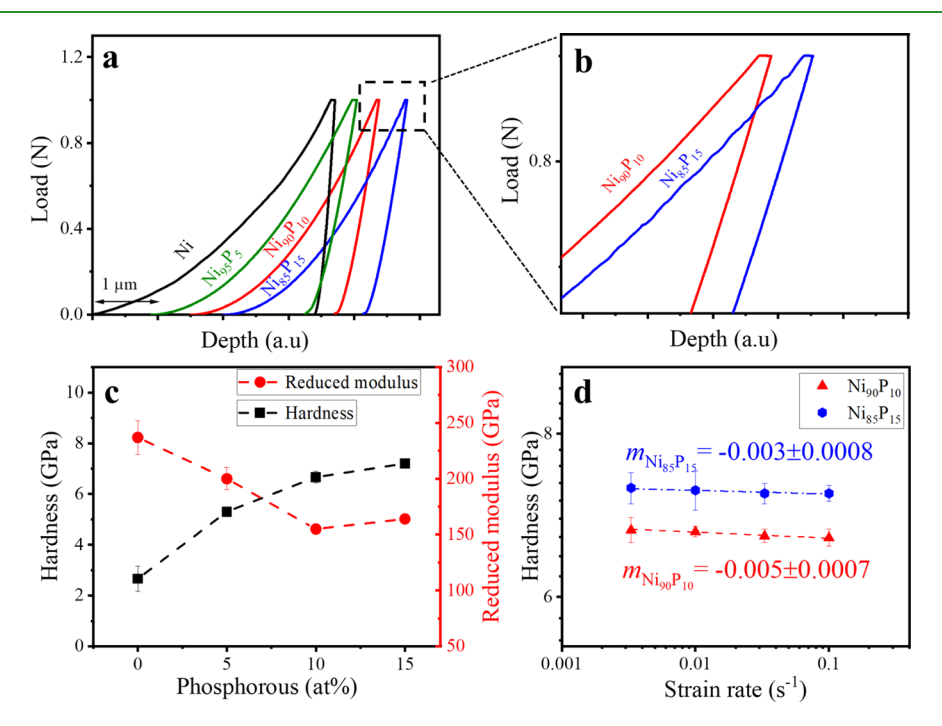


Figure 3. Mechanical behavior of the electrodeposited alloys: (a) nanoindentation load—displacement plots for the Ni–P electrodeposited alloys; (b) zoomed-in view of the selected part in (a) showing serrated behavior for  $Ni_{85}P_{15}$  and the relatively smooth curve for  $Ni_{90}P_{10}$ ; (c) hardness and modulus as a function of P content for all the alloys, indicating higher hardness and lower modulus for the amorphous alloys; (d) hardness vs strain rate in the double logarithmic scale showing negative strain rate sensitivity (m) for the two EMGs,  $Ni_{85}P_{15}$  and  $Ni_{90}P_{10}$ , with the values indicated alongside the curves.

electrodeposited alloys is shown in Figure 2. X-ray diffraction (XRD) spectra for all the electrodeposited bulk alloys are shown in Figure 2a. Electrodeposited pure Ni showed a set of sharp diffraction peaks indexed as (111), (200), and (220). Ni<sub>95</sub>P<sub>5</sub> showed slightly broader peaks, indicating the nanocrystalline structure. A further increase in phosphorous content to the range of 10–15 at. % resulted in broad diffraction peaks

indicative of the amorphous structure for these alloys. However, electrodeposited  $Ni_{75}P_{25}$  showed crystalline peaks with the formation of the  $Ni_3P$  intermetallic compound. Differential scanning calorimetry (DSC) analysis of the amorphous Ni–P alloys with phosphorous contents of 10 and 15 at. % is shown in Figure 2b. The glass transition temperature ( $T_g$ ) for the two alloys was in the range of 310–

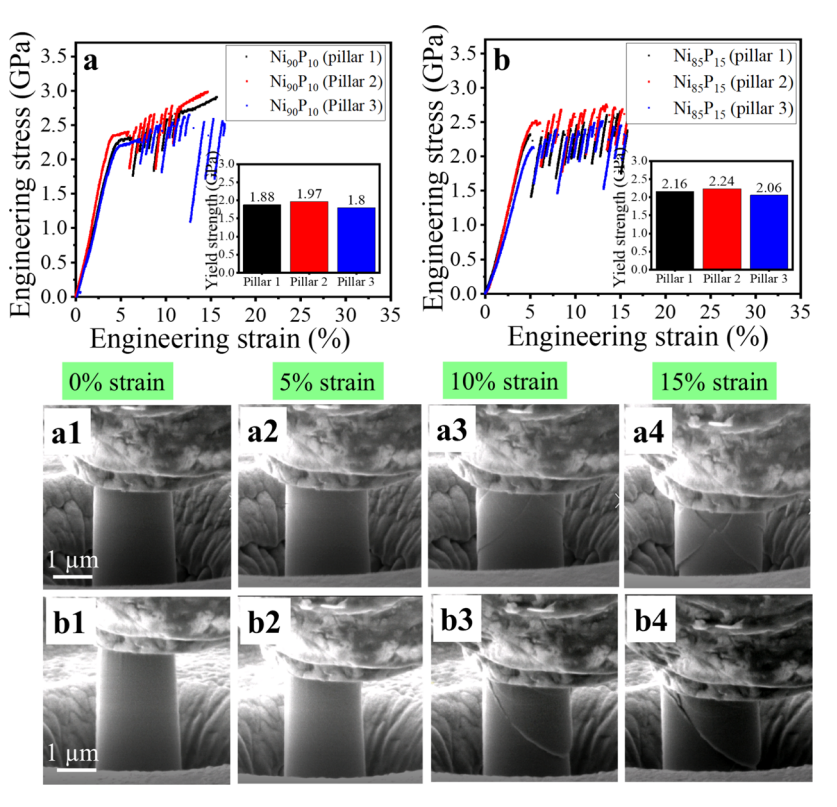


Figure 4. Micropillar compression and deformation behavior of  $Ni_{90}P_{10}$  vs  $Ni_{85}P_{15}$  metallic class: engineering stress—strain curve for (a)  $Ni_{90}P_{10}$  and (b)  $Ni_{85}P_{15}$  electrodeposited alloys, and yield strength obtained at 0.2% offset is shown as insets, indicating increasing yield strength with increasing P content. Three pillars were tested for each alloy as shown. Serration flow or load drop as characteristic of amorphous alloys due to shear band nucleation and propagation is evident for electrodeposited Ni–P metallic glasses;  $Ni_{90}P_{10}$  showed larger strain before first catastrophic load drop, indicating its better plasticity and homogeneous flow. In situ SEM image at strains of 0, 5, 10, and 15% of micropillars of  $[a(1-4)]Ni_{90}P_{10}$  and  $[b(1-4)]Ni_{85}P_{15}$  electrodeposited alloys after compression, indicating multiple shear band formation for  $Ni_{90}P_{10}$  in comparison to other amorphous alloys which deformed with one major shear band.

315 °C, while crystallization temperature  $(T_x)$  was in the range of 340-350 °C. The inset shows the DSC plot around the melting point for the two alloys with the solidus temperature determined to be in the range of 870-880 °C, in agreement with the Ni-P phase diagram. 14 Synthesis of amorphous alloys using the electrodeposition process seems favorable for compositions around the deep eutectic similar to the criterion for glass formation by melt quenching. High-resolution transmission electron microscopy (HRTEM) and selected area electron diffraction (SAED) patterns for Ni<sub>90</sub>P<sub>10</sub> and Ni<sub>85</sub>P<sub>15</sub> bulk alloys supported their amorphous structure with no discernible difference between the two compositions (Figure 2c). There was no indication of nanoglass formation in both the alloys, as reported previously for amorphous alloys obtained by magnetron sputtering. 15 Bright-field transmission electron microscopy (BFTEM) and HRTEM and SAED patterns for Ni<sub>85</sub>P<sub>15</sub> nanowires are also shown in Figure 2d,e, respectively, confirming the amorphous structure of the nanowires. The TEM sample preparation was carried out at very low current (~70 pA) to prevent sample preparationinduced crystallization.

For pulsed electrodeposition at high overpotentials as used in this study, the constituent atoms rapidly discharge on the substrate with little time to assume thermodynamically dictated periodicity, thereby leading to the amorphous structure. The microstructures obtained from the electrodeposition process for pure Ni and Ni–P are schematically shown in Supporting Information, Figure S4. For a small amount of alloying, phosphorus gets incorporated into the

octahedral interstitial sites of face-centered cubic (FCC) nickel in the Ni–P system. However, increasing phosphorus content in the range of 10–15 at. % frustrates the thermodynamically predicted crystalline phase of  $Ni_3P$  and FCC Ni solid solution and results in amorphization.  $^{8,16}$ 

Mechanical Behavior. Nanoindentation load-displacement (P-h) curves for the electrodeposited alloys at a maximum load of 1000 mN are shown in Figure 3a,b. The hardness (H) and modulus (E) determined from P-h curves are shown in Figure 3c. The EMGs showed three times higher hardness and ~35% lower modulus compared to electrodeposited pure Ni. The lower modulus or stiffness of metallic glasses compared to their crystalline counterparts is attributed to weaker atomic bond strength and less dense packing of atoms in the amorphous structure. 17,18 The average hardness increased with the increase in P content from 5 to 15 at. % in the order  $Ni_{95}P_5$  ( $H \sim 5.3$  GPa) <  $Ni_{90}P_{10}$  ( $H \sim 6.66$  GPa) <  $Ni_{85}P_{15}$  ( $H \sim 7.2$  GPa). The pop-ins or serrations in the load displacement curves were more pronounced in the alloy with 15 at. % P, while the indentation curve for Ni<sub>90</sub>P<sub>10</sub> was relatively smooth, indicating more homogeneous flow (Figure 3b). The degree of pop-in was insignificant for Ni<sub>90</sub>P<sub>10</sub>, while it was in the range of  $\sim$ 5-15 nm for Ni<sub>85</sub>P<sub>15</sub>. Serrated flow has been correlated with shear banding in metallic glasses to accommodate plastic strain.  $^{19-21}$  Yielding and plasticity in amorphous alloys proceed by localization of large shear strain in relatively narrow bands (~20 nm) during deformation at temperatures below the glass transition.<sup>21</sup> Higher magnitude and frequency of pop-ins for Ni<sub>85</sub>P<sub>15</sub> indicate larger shear

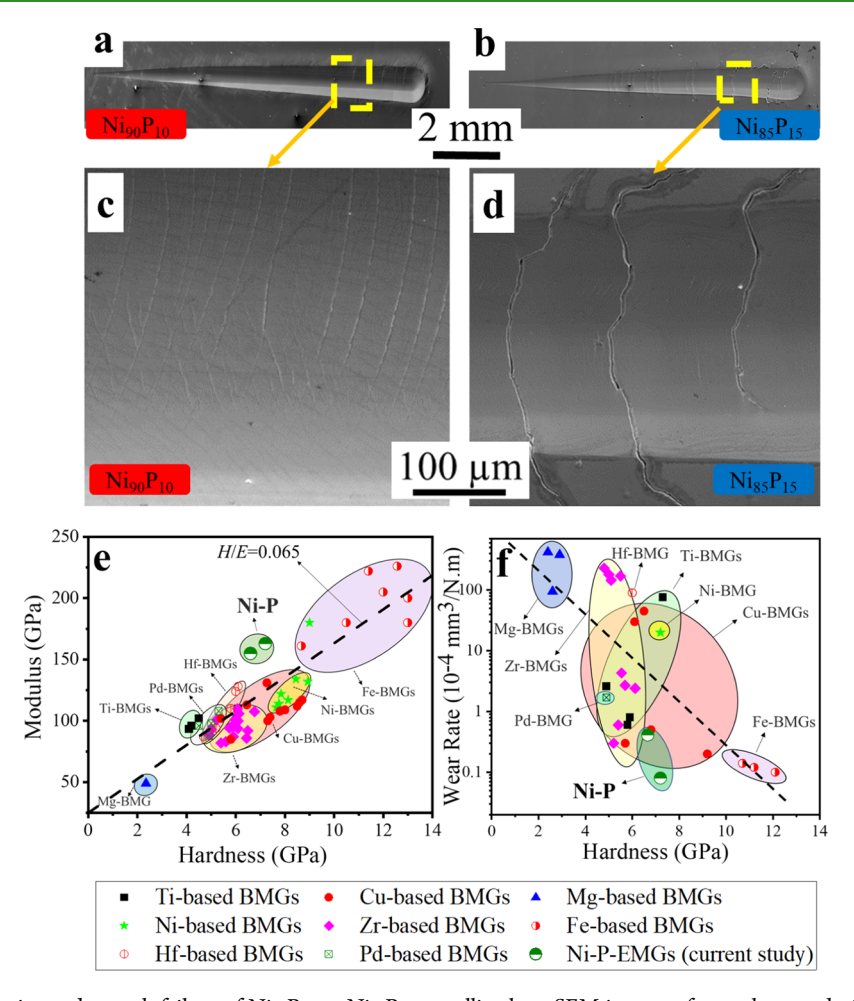


Figure 5. Tribological behavior and scratch failure of  $Ni_{90}P_{10}$  vs  $Ni_{85}P_{15}$  metallic glass: SEM images of scratch scars during progressive scratch test of (a,c)  $Ni_{90}P_{10}$  and (b,d)  $Ni_{85}P_{15}$  showing ductile behavior for  $Ni_{90}P_{10}$  and relatively brittle behavior for  $Ni_{85}P_{15}$ ; Ashby plot comparing mechanical and tribological properties of several reported BMGs and the two studied Ni–P EMGs: (e) modulus vs hardness<sup>2,29–45</sup> along with a dashed trend line for H/E = 0.065; (f) wear rate vs hardness<sup>47–55</sup> along with a dashed trend line for inverse relationship between the wear rate and hardness; the current Ni–P EMGs showed higher hardness and lower wear rate compared to most BMGs.

displacement and more localized deformation compared to the  $\mathrm{Ni}_{90}P_{10}$  alloy.  $^{20,22}$  The hardness values as a function of strain rate at a depth of 3000 nm for Ni<sub>90</sub>P<sub>10</sub> and Ni<sub>85</sub>P<sub>15</sub> are shown in Figure 3d in double logarithmic scales. Softening of the EMGs was observed with the increase in applied strain rate. Strain rate sensitivity, m, was calculated from the slope of linear fitting of the data<sup>23</sup> and indicated alongside the curves in Figure 3d. Negative strain rate sensitivity was found for both the electrodeposited amorphous alloys. A similar behavior has been reported for several bulk metallic glasses and attributed to the free volume generated at higher strain rates.<sup>24</sup> The Ni<sub>90</sub>P<sub>10</sub> alloy showed roughly two times larger absolute m value as compared with Ni<sub>85</sub>P<sub>15</sub> EMG, suggesting more homogeneous plastic flow.<sup>25</sup> This is consistent with the smooth loaddisplacement curves for Ni<sub>90</sub>P<sub>10</sub> compared to the serrated behavior seen for Ni<sub>85</sub>P<sub>15</sub> in Figure 3b. A shear transformation involves local rearrangement of atomic clusters which accommodate plastic strain in response to applied stress over a region referred to as the shear transformation zone (STZ). Local aggregation of STZs lead to shear band nucleation, and STZ volume provides estimate of the number of atoms involved in shear transformation in a metallic glass.<sup>21</sup> STZ volume calculated based on the Johnson-Sawmer cooperative shearing model (CSM)<sup>26</sup> was 6.5 and 10 nm<sup>3</sup> for Ni<sub>90</sub>P<sub>10</sub> and

 $Ni_{85}P_{15}$ , respectively. Smaller STZ volume and higher density of STZs for  $Ni_{90}P_{10}$  enable more flow units to be activated for shear band nucleation and promote relatively ductile behavior compared to the  $Ni_{85}P_{15}$  alloy.<sup>27,28</sup>

Stress-Strain and Deformation Behavior of Ni<sub>90</sub>P<sub>10</sub> **Versus** Ni<sub>85</sub>P<sub>15</sub> Metallic Glass. The engineering stress—strain responses obtained from micropillar compression for Ni<sub>90</sub>P<sub>10</sub> and Ni<sub>85</sub>P<sub>15</sub> alloys are shown in Figure 4a,b, respectively. For each alloy, three individual micropillars were tested as shown. The yield strengths were calculated at 0.2% offset and are shown as insets in Figure 4. The average value of yield strength for  $Ni_{85}P_{15}$  was ~2.16 GPa, while for  $Ni_{90}P_{10}$ , it was ~1.88 GPa. The large load drops in stress-strain curves for the two alloys after the yield point was attributed to the nucleation and propagation of shear bands. 19 The stress-strain curves demonstrated a brittle type of failure for Ni<sub>85</sub>P<sub>15</sub>, while Ni<sub>90</sub>P<sub>10</sub> showed relatively more plasticity. The plastic strain before the first load drop was  $\sim$ 4% for Ni<sub>90</sub>P<sub>10</sub>, and it was close to zero for Ni<sub>85</sub>P<sub>15</sub>. The in situ SEM images of the micropillars at strains of 0, 5, 10, and 15% are shown in Figure 4a(1-4),b(1-4) for Ni<sub>90</sub>P<sub>10</sub> and Ni<sub>85</sub>P<sub>15</sub>, respectively. The in situ videos of micropillar compression for the two alloys are uploaded as the Supporting Information (Supporting Information, Video S1 and Supporting Information, Video S2).

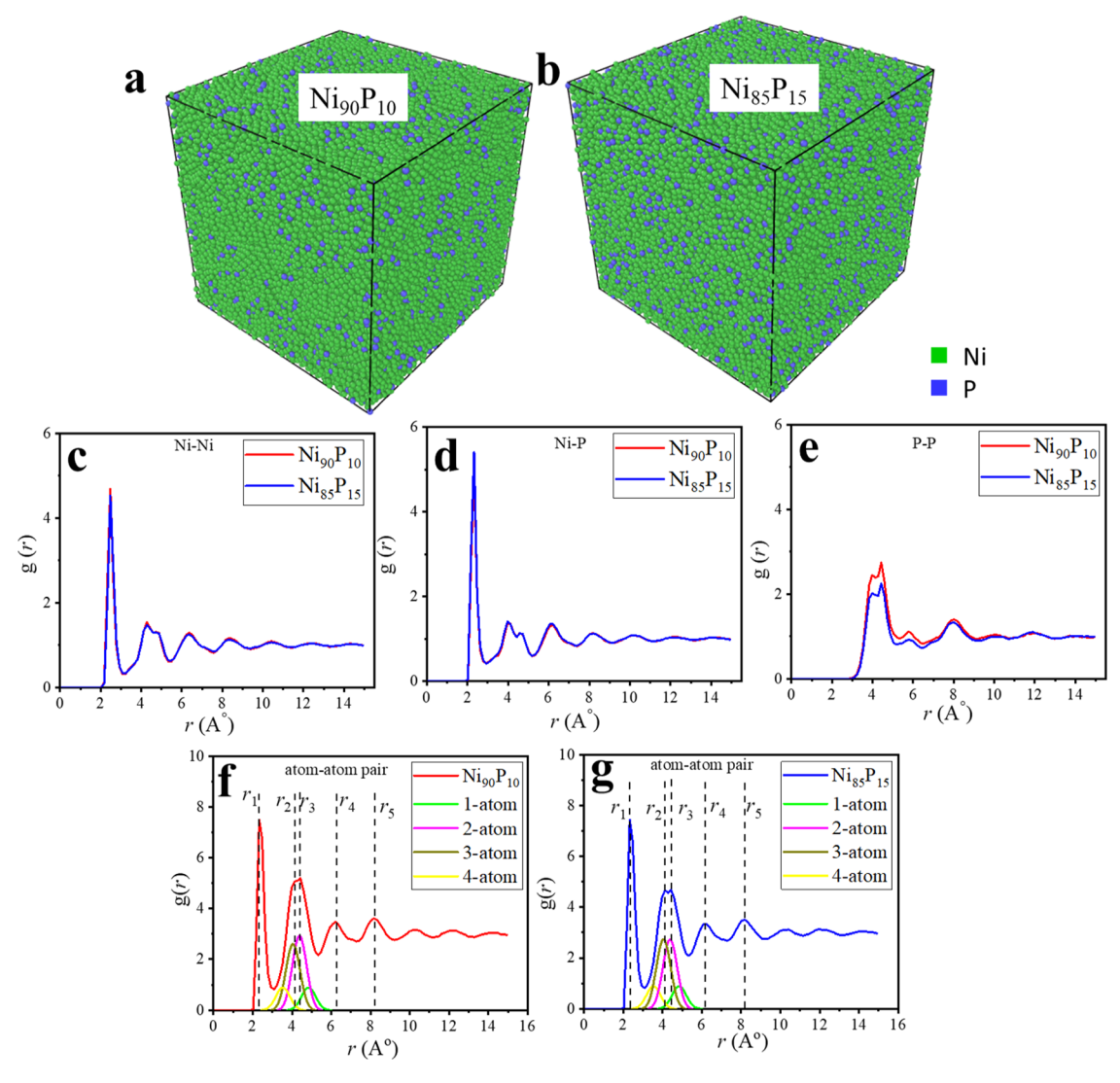


Figure 6. Atomic configurations and radial distribution function for  $Ni_{90}P_{10}$  vs  $Ni_{85}P_{15}$  metallic glass using MD simulation: 3D atomic configuration of MD simulated (a)  $Ni_{90}P_{10}$  and (b)  $Ni_{85}P_{15}$ ; the green and blue circles represent Ni and P atoms, respectively. The partial RDFs of both MD simulated Ni–P metallic glasses for the (c) Ni–Ni pair, (d) Ni–P pair, and (e) P–P pair at room temperature. The total atom–atom pair RDF of (f)  $Ni_{90}P_{10}$  and (g)  $Ni_{85}P_{15}$  with the peak positions shown as dashed vertical lines. The deconvoluted RDF for each of the connection schemes are presented, indicating stronger two-atom connection for  $Ni_{90}P_{10}$  and two-atom and three-atom connection for  $Ni_{85}P_{15}$ .

The micropillars for  $Ni_{85}P_{15}$  failed by a single major shear band, while  $Ni_{90}P_{10}$  micropillars showed multiple shear bands consistent with the observed stress—strain response. Activation of multiple shear bands helped in plasticity accommodation in the case of  $Ni_{90}P_{10}$ , resulting in the overall higher ductility compared to  $Ni_{85}P_{15}$  EMG. Greater plasticity in amorphous alloys is typically obtained if deformation is accommodated by a higher fraction of more closely spaced shear bands due to higher energy dissipation. Plastic flow may begin easily on preexisting shear bands, leading to more distributed shear and inhibition of catastrophic failure. <sup>21</sup>

Wear Rate and Scratch Failure of  $Ni_{90}P_{10}$  Versus  $Ni_{85}P_{15}$  Metallic Glass. Tribological properties of  $Ni_{90}P_{10}$  and  $Ni_{85}P_{15}$  EMGs were studied using the reciprocating wear and unidirectional scratch test. The average coefficient of friction sliding against the AISI 52100 steel counterface at a frequency of 10 Hz and a load of 5 N was ~0.45 for both alloys. The wear rate for the  $Ni_{90}P_{10}$  alloy was  $4.1 \times 10^{-5}$  mm<sup>3</sup>/N·m, while that for  $Ni_{85}P_{15}$  was  $0.8 \times 10^{-5}$  mm<sup>3</sup>/N·m. Figure 5a–d shows the SEM images of both EMGs after progressive scratch tests.

Series of nested microcracks were observed on the scratch scar for Ni<sub>90</sub>P<sub>10</sub>, as shown in Figure 5a, and the corresponding higher magnification image is shown in Figure 5c. These cracks were limited only to the scratch scar and not fully developed outside the scratch. However, the cracks for Ni<sub>85</sub>P<sub>15</sub> were fully developed and propagated outside the grooves (Figures 5b,d). These findings further support the ductile behavior of Ni<sub>90</sub>P<sub>10</sub> EMG in contrast to the brittle behavior seen for the Ni<sub>85</sub>P<sub>15</sub> alloy, in agreement with the nanomechanical experiments. Figure 5e shows the Vickers hardness (*H*) versus modulus (*E*) of several reported bulk metallic glasses (BMGs)<sup>2,29-45</sup> along with the two EMGs developed in this study. Linear correlation between hardness and modulus ( $H/E \approx 0.05-0.065$ ) has been reported previously,<sup>46</sup> and a similar correlation is shown by a dashed line in Figure 5e. The hardness of the current Ni-P EMGs was in the same range as reported for Ni-based bulk metallic glasses<sup>33</sup> but significantly higher than other bulk glassforming systems including Ti-based BMGs, 30,38 Zr-based BMGs, 38,40,44 and Pd-based BMGs. 35-37,44 Wear rate versus hardness for all reported BMGs and two studied EMGs is

Table 1. Atomic Peak Positions Measured from g(r), Average Coordination Number (CN) Around P Solute Center Atoms, and Fraction of Polyhedra (BSAP) for Ni-P Metallic Glasses Obtained from MD Simulation at Room Temperature

| alloy           | $r_1$ (Å) | $r_2$ (Å) | $r_3$ (Å) | $r_4$ (Å) | $r_5$ (Å) | average CN (P-Ni) | average CN (P-P) | BSAP fraction (%) |
|-----------------|-----------|-----------|-----------|-----------|-----------|-------------------|------------------|-------------------|
| $Ni_{90}P_{10}$ | 2.32      | 4.12      | 4.42      | 6.26      | 8.19      | 10.91             | 9.74             | 27.1              |
| $Ni_{85}P_{15}$ | 2.32      | 4.12      | 4.42      | 6.13      | 8.18      | 10.86             | 10.29            | 29.8              |

shown in Figure 5f.<sup>47–55</sup> Inverse correlation between hardness and wear rate is shown in Figure 5f as a trend (dashed) line per Archard's relationship.<sup>56</sup> Mg-based BMGs showed the highest wear rate, and Fe-based BMGs exhibited the lowest wear rate. The wear rate for Ni<sub>90</sub>P<sub>10</sub> and Ni<sub>85</sub>P<sub>15</sub> EMGs was comparable to that of Fe-based BMGs. The high hardness and strength and very low wear rates for the two studied Ni–P EMGs suggest their potential use in many structural and tribological applications.

Local Atomic Ordering in Ni<sub>90</sub>P<sub>10</sub> Versus Ni<sub>85</sub>P<sub>15</sub> Metallic Glass. The X-ray diffraction peak positions, highresolution transmission electron microscopy images, and SAED patterns for Ni<sub>90</sub>P<sub>10</sub> and Ni<sub>85</sub>P<sub>15</sub> metallic glasses were very similar and showed no discernible difference. Therefore, MD simulations were carried out for understanding the local atomic order to explain the distinct differences seen in the deformation and scratch behavior of the two amorphous alloys, Ni<sub>90</sub>P<sub>10</sub> and Ni<sub>85</sub>P<sub>15</sub>. There are no reports on local atomic structure changes as a function of composition for the Ni-P amorphous system. Increased local atomic ordering and lower fraction of fertile sites for STZ nucleation in metallic glass may make it more prone to localized plastic deformation. 19,57,58 Three-dimensional (3D) atomic configurations for the two amorphous alloys were determined by MD simulation, and the radial distribution function (RDF), g(r), was calculated at room temperature as<sup>55</sup>

$$g(r) = \frac{L^3}{N} \left\langle \left( \sum_{1}^{N} n(r) \right) / 4\pi r^2 dr \right\rangle$$
 (1)

where L is the box size, N is the number of atoms, and n(r) is the number of atoms at the nearest neighboring distance r. Figure 6a,b shows the atomic configurations for Ni<sub>90</sub>P<sub>10</sub> and  $Ni_{85}P_{15}$ , respectively. The radial distribution function, g(r), gives the probability of finding atoms at a given distance from the center atom. 59 The position and relative intensity of the peaks provide quantitative estimate of short-to-medium range ordering in amorphous alloys. 58,60 The first peak in RDF corresponds to short-range ordering (SRO), whereas the structural features beyond the first peak are indicative of medium-range ordering (MRO).<sup>58</sup> Figure 6c–g shows the g(r)obtained from MD simulation for Ni<sub>90</sub>P<sub>10</sub> and Ni<sub>85</sub>P<sub>15</sub> EMGs for large atomic separation (~15 Å) to demonstrate how the atomic structure evolves with the change in composition. Figure 6c-e illustrates the partial g(r) for two Ni-P EMGs, showing nearest average interatomic distances for the Ni-Ni, Ni-P, and P-P pairs, respectively. The first peak in the P-P partial RDF was absent for both compositions, suggesting that P atoms do not appear to be nearest neighbors of each other (P-P avoidance). The overall g(r) for  $Ni_{90}P_{10}$  and  $Ni_{85}P_{15}$ after summing the contributions of the partial RDFs is shown in Figure 6f,g. Five pronounced peaks were present in the range of ~15 Å, indicating short to medium range structural ordering in Ni-P metallic glasses. Peak positions were determined by Gaussian fitting to the g(r) curves. The first peak position for the two studied Ni-P EMGs was located at

2.32 Å, confirming that g(r) of the alloys was dominated by the Ni-P pairs (Figure 6d). The first peak position represents the distance between one Ni and one P atom with atomic radii of 1.25 and 1.10 Å 61, respectively, and the atomic pair distance of Ni-P did not change with alloy composition. All the peak positions  $(r_i; i = 1, 2, 3, 4, \text{ and } 5)$  representing the average distance from the ith nearest neighbor to the center atom are shown by vertical dashed lines in Figure 6f,g and summarized in Table 1. The values of  $r_i/r_1$  (i = 1, 2, 3, 4, and 5) were measured to be ~1.0, 1.77, 1.9, 2.67, and 3.53, which may be approximated as  $\sqrt{1}$ ,  $\sqrt{3}$ ,  $\sqrt{4}$ ,  $\sqrt{7}$ , and  $\sqrt{12}$ . These constants are the global features of RDFs, regardless of chemical composition originating from the spherical periodic order (SPO) combined with local translational symmetry (LTS) in metallic glasses. 59,62 Values of  $\sqrt{1}$ ,  $\sqrt{3}$ ,  $\sqrt{7}$ , and  $\sqrt{12}$  are predicted from SPO, whereas the value of  $\sqrt{4}$  arises from the crystalline-like order (LTS). Therefore, atomic packing in these metallic glasses may be considered to be superimposition of LTS on the SPO.<sup>62'</sup> Splitting of the second RDF peak observed in g(r) for both studied Ni-P EMGs may be related to the distribution of different types of cluster connections and the medium-range order.  $^{62-65}$  The position and intensity of the split peaks may vary with the change in ordering and cluster connection. There are four different kinds of cluster connections, namely, one-atom connection (vertex-shared), two-atom connection (edge-shared), three-atom connection (face-shared), and four-atom connection (sharing of distorted quadrilateral or squashed tetrahedra). 65 Each of these connections results in subpeaks in g(r) at different correlation distances. An amorphous alloy with more structural ordering shows relatively higher fraction of three-atom connections compared to two-atom and four-atom connections. 65 The deconvoluted RDFs for each of the connection schemes for Ni-P metallic glasses are shown in Figure 6f,g. The second nearest-neighbor position in the Ni-P amorphous alloy was found to be 4.84 Å for one-atom connection, 4.38 Å for twoatom connection, 4.05 Å for three-atom connection, and 3.53 Å for four-atom connection. 65 The calculated subpeak positions (summarized in Table 1) indicate that the type of cluster connection changed as P content was increased from 10 to 15 at. %. For  $Ni_{90}P_{10}$ , the peak at ~4.42 Å showed slightly higher intensity, indicating a higher fraction of two-atom cluster connections. For Ni<sub>85</sub>P<sub>15</sub>, the peaks at 4.42 Å and 4.12 Å showed roughly equal intensities, indicating equal fractions of two-atom and three-atom cluster connections. The clusters with two-atom connection are more flexible as their local deformation exceeds the macroscopic strain, whereas clusters with three-atom connection are stiffer. 65 The local increase in stiffness with higher proportion of three-atom connection may hinder multiple shear-band formation and increase the strength. Thus, experimentally observed higher yield strength and lower plastic strain for Ni<sub>85</sub>P<sub>15</sub> (Figure 4b) may be attributed to the higher fraction of three-atom cluster connections. However, Ni<sub>90</sub>P<sub>10</sub> with a higher fraction of twoatom cluster connection may favor STZ nucleation and show

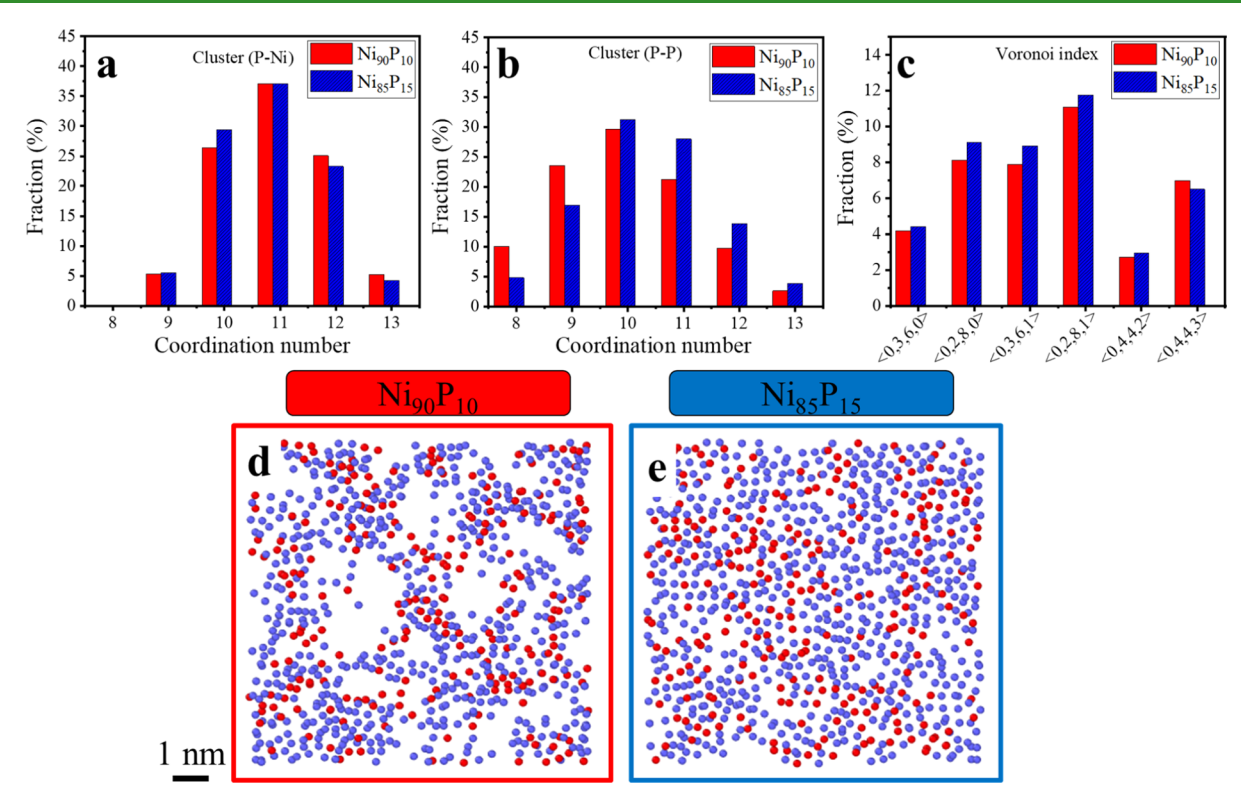


Figure 7. Polyhedra cluster characterization for  $Ni_{90}P_{10}$  vs  $Ni_{85}P_{15}$  metallic glass using MD simulation: fraction of clusters with different CNs for the (a) P–Ni pair and (b) P–P pair; (c) histogram of Voronoi polyhedra with P as the center atom showing the dominant coordination polyhedra of  $\langle 0,2,8,1 \rangle$ ,  $\langle 0,3,6,1 \rangle$ , and  $\langle 0,2,8,0 \rangle$ . Spatial distribution of SRO clusters within a length scale of 5 Å in (d)  $Ni_{90}P_{10}$  and (e)  $Ni_{85}P_{15}$ , showing more packed atomic configuration in  $Ni_{85}P_{15}$  compared to  $Ni_{90}P_{10}$ . Red circles represent BSAP or similar structures, and blue circles indicate other kinds of structures.

relatively more plastic strain prior to failure, as depicted in Figure 4a.

Solute-centered clusters are the fundamental building blocks of the short-range order in metallic glasses. 66 The fraction of clusters with different coordination numbers (CNs) for the P-Ni pair and P-P pair are shown in Figure 7a,b, respectively. The average CNs for P-Ni and P-P pairs for both EMGs are summarized in Table 1. The CN for P-Ni clusters ranged from 9 to 13 with an average of 10.91 for Ni<sub>90</sub>P<sub>10</sub> and 10.86 for Ni<sub>85</sub>P<sub>15</sub>. The average CN around the phosphorus atom in  $Ni_{80}P_{20}$  has been reported to be ~10.5. S8,61 For P-P, on the other hand, the average CN was 9.74 and 10.29 for Ni<sub>90</sub>P<sub>10</sub> and Ni<sub>85</sub>P<sub>15</sub>, respectively (summarized in Table 1). With the increase in solute (phosphorus) concentration, the fraction of solute-solute bonds increased. 67 The average CN is related to the effective size ratio between the solute atom and the solvent atom. 61 Small solute atoms may accommodate fewer solvent atoms in the first coordination shell, whereas more solvent atoms may surround a larger solute atom in the first coordination shell. Size ratios of 0.902 and 0.835 correspond to the ideal icosahedral (CN = 12) and bicapped square antiprism (BSAP) (CN = 10) atomic packing, respectively. <sup>61,67</sup> For the two amorphous Ni-P EMGs, the effective size ratio between Ni and P was estimated by  $(D_{Ni-P}-D_{Ni-Ni}/2)/(D_{Ni-Ni}/2)$ 2), where D<sub>Ni-P</sub> and D<sub>Ni-Ni</sub> are bond distances between Ni-P (2.32 Å) and Ni-Ni (2.47 Å), respectively, found from their partial RDFs in Figure 6c,d, respectively. The effective size ratio between Ni and P was found to be ~0.87 for both alloys which is between 0.902 for CN = 12 and 0.835 for CN = 10, suggesting that CN of ~11 may be considered as distorted BSAP 61. The topology of solute-centered clusters in the MD-

simulated MGs was investigated by the Voronoi spatial tessellation technique,  $^{68}$  as shown in Figure 7c. The Voronoi index is used to distinguish between different kinds of coordination polyhedra clusters (i.e., SROs) and several clusters may coexist in the amorphous alloys.<sup>67</sup> Here, only those with a fraction larger than 2% were selected. Figure 7c shows the distribution of major Voronoi polyhedra with P as the center atom. The dominant polyhedra were the ones with a Voronoi index of (0,2,8,1) (CN = 11) followed by (0,2,8,0)(CN = 10) and (0,3,6,1) (CN = 10). All the structures correspond to BSAP (CN = 10) or distorted BSAP (CN = 11), which are distinctly different from icosahedral SRO common to many metallic glasses. 61 The fraction of BSAP or distorted BSAP polyhedra were  $\sim$ 27.1 and 29.8% in Ni<sub>90</sub>P<sub>10</sub> and Ni<sub>85</sub>P<sub>15</sub>, respectively (included in Table 1). The Voronoi index (0,2,8,1) polyhedron may also be a distorted icosahedron with one atom missing from the icosahedral packing.<sup>58</sup> In addition, clusters with a Voronoi index of (0,3,6,0) (CN = 9), which corresponds to tricapped trigonal prism (TTP) packing, occupied 4-7% of total polyhedra. The spatial distribution of these clusters for each of the two amorphous alloys is shown in Figure 7d,e. Red circles represent BSAP and similar SRO structures, and the blue ones represent all other structures. The degree of structural heterogeneity is clearly different in the two alloys which may explain the difference in their experimentally observed mechanical and scratch behavior. Figure 7d,e indicates that the increase in phosphorus content (from Ni<sub>90</sub>P<sub>10</sub> to Ni<sub>85</sub>P<sub>15</sub>) increased the fraction of polyhedra clusters (SROs) locally, which leads to higher stiffness, modulus, and yield strength. Regions without any short-range order have been referred to as "geometrically unfavorable motifs"

(GUMs) or "liquid-like" regions that show lower stiffness and may act as favorable sites for shear transformation, leading to homogeneous plasticity. 57,69 Figure 7d shows less SRO clusters and more GUMs for Ni<sub>90</sub>P<sub>10</sub> EMG, while a lower fraction of GUMs was observed for the  $Ni_{85}P_{15}$  alloy (Figure 7e). In sum, the increase in phosphorus content going from Ni<sub>90</sub>P<sub>10</sub> to Ni<sub>85</sub>P<sub>15</sub> resulted in a larger fraction of BSAP polyhedra clusters. In addition, the connectivity between BSAP-ordered clusters (i.e., MRO) increased, mainly through face sharing, resulting in a compact, stable, and strong network structure. This likely explains the higher hardness, modulus, and strength but reduced plasticity going from Ni<sub>90</sub>P<sub>10</sub> to Ni<sub>85</sub>P<sub>15</sub>, seen experimentally in Figures 3 and 4. A similar behavior has been reported for Al addition in Zr-Ni-Al metallic glasses<sup>10</sup> and the increase in Zr fraction in Cu-Zr metallic glasses.<sup>58</sup> The increase in Al content increased Al-centered icosahedral clusters for Zr-Ni-Al metallic glasses, resulting in strengthening and embrittlement.<sup>10</sup> In Supporting Information Figure S5a, engineering stress-strain curves for the MD-simulated Ni-P alloys obtained from uniaxial compression tests are compared. The yield strength measured at 0.2% offset increased with increasing P content, in agreement with experimental data (Supporting Information, Figure S5b).

## MATERIALS AND METHODS

**Alloy Synthesis.** Ni<sub>100-x</sub>P<sub>x</sub> (x = 0, 5, 10, 15, and 25 at. %) alloys were synthesized using pulsed electrodeposition with a pulse power supplier (Dynatronix-MicroStar) in a modified Watt's bath containing phosphorous acid (H<sub>3</sub>PO<sub>3</sub>) at ~40 °C and a pH of 1.8. The electrolyte composed of a mixture of nickel sulfate [NiSO<sub>4</sub>·6H<sub>2</sub>O (365 g/L)], nickel chloride [NiCl<sub>2</sub>·6H<sub>2</sub>O (32 g/L)], phosphorous acid [H<sub>3</sub>PO<sub>3</sub> (20 g/L)], boric acid [H<sub>3</sub>BO<sub>3</sub> (40 g/L)], and sodium dodecyl sulfate [NaC1<sub>2</sub>H<sub>25</sub>SO<sub>4</sub> (0.4 g/L)]. Electrodeposition was carried out on the pure copper substrate used as the cathode and a pure nickel (99.99%) plate used as the soluble anode. Chemical activation of the substrate was carried out in 1:5 sulfuric acid (H<sub>2</sub>SO<sub>4</sub>) for 10 s. NiSO<sub>4</sub> was the primary source of nickel, while NiCl<sub>2</sub> helped in increasing solution conductivity, active dissolution of the nickel anode, and uniformity of the coating thickness.8 An electrolyte containing H<sub>3</sub>PO<sub>3</sub> is very acidic due to the discharge of H<sup>+</sup> ions, so partial neutralization was necessary to increase the pH value of the bath to an optimum value. Therefore, H<sub>3</sub>BO<sub>3</sub> was added to control the pH.8 In addition, sodium dodecyl sulfate was used in the electrolyte as a wetting agent to control pitting. The bath was stirred with a magnetic agitator during deposition. The applied duty cycle [d.c. =  $t_{\rm on}/(t_{\rm on} + t_{\rm off})$ , where  $t_{\rm on}$  is the pulsing time and  $t_{\rm off}$  is the relaxation OFF time] and pulse frequency were 0.5 and 100 Hz, respectively. All other conditions including temperature, pH, electrolyte composition, and agitation rate were kept constant. The peak current density (ip) was varied to obtain electrodeposited Ni-P alloys with phosphorus contents of 0, 5.0  $\pm$  0.2, 10.0  $\pm$  0.2, 15.0  $\pm$ 0.5, and 25.0  $\pm$  0.5 at. %. The peak current density was 20 A/dm<sup>2</sup> for  $Ni_{95}P_{5}$ , 17 A/dm<sup>2</sup> for  $Ni_{90}P_{10}$ , 12 A/dm<sup>2</sup> for  $Ni_{85}P_{15}$ , and 5 A/dm<sup>2</sup> for Ni<sub>75</sub>P<sub>25</sub>. The deposition time was set to 0.5-4 h to obtain alloys with a desired thickness. The bath temperature and pH were monitored and regulated in order to avoid composition variation over long periods of time for thicker deposits. Commercially available anodic aluminum oxide (AAO) nanomolds were used as templates for the synthesis of amorphous Ni-P nanowires. The templates were dissolved in an alkaline solution to obtain the nanowires in the free-standing form.

Microstructural Characterization and Thermal Analysis. Structural characterization was carried out using an X-ray diffractometer (XRD, Bruker, USA) with 1.54 Å wavelength Cu-K $\alpha$  radiation. Transmission electron microscopy (TEM) was carried out on an FEI Tecnai F20 operating at 200 kV. Samples were prepared using FEI Nova NanoLab 200 focused ion beam SEM (FIB-SEM) at

a voltage of 5 kV and 70 pA current. Final thinning was performed at the lowest voltage and current to reduce Ga ion beam damage. The cross-sectional microstructure and elemental distribution were measured using SEM (FEI, Hillsboro, OR, USA) equipped with EDS. Thermal analysis of the samples was carried out using differential scanning calorimetry (DSC, SDT Q600) in the temperature range of 25–1400 °C and a heating and cooling rate of 20 °C/min. Heat flow calibration was carried out based on two runs including empty pan and a sapphire disc. Inert argon gas at a flow rate of 20  $\mu L/min$  was used to prevent oxidization of the samples.

**Nanoindentation.** Nanoindentation was performed using a TI-Premier Triboindenter (Bruker, Minneapolis, MN, USA) with a diamond Berkovich tip at room temperature with a maximum load of 1000 mN to determine the hardness and modulus using the Oliver and Pharr method. <sup>70</sup> Each data point was obtained from an average of 12 indents with 100  $\mu$ m spacing between two indents to avoid overlap of their plastic zones. The thermal drift rate was maintained below 0.05 nm/s for all tests. Strain rate sensitivity (SRS) was calculated by nanoindentation in the displacement-control mode with applied strain rates of  $3.0 \times 10^{-3}$ ,  $1.0 \times 10^{-2}$ ,  $3.0 \times 10^{-2}$ , and  $1.0 \times 10^{-1}$  s<sup>-1</sup>.

**Micropillar Compression.** Pillars with an aspect ratio of 2 ( $\sim$ 5  $\mu$ m height and  $\sim$ 2.5  $\mu$ m diameter) were milled in the electrodeposited alloys using an FEI Nova NanoLab 200 FIB-SEM instrument in several steps using Ga beam current ranging from 5 nA to 10 pA. The top and bottom diameter of the micropillars were calculated, and the taper angle was determined to be <2°. The top diameter was used to calculate the cross-sectional area of each micropillar. Micropillar compression tests were performed in a PI88 SEM PicoIndenter (Bruker, Minneapolis, MN, USA) with a 5  $\mu$ m diameter flat diamond punch in the displacement-control mode at a strain rate of  $\sim$ 6 × 10<sup>-3</sup> s<sup>-1</sup>. The recorded load versus displacement was converted to the engineering stress—strain curve. At least three micropillars were milled for each alloy to determine the standard deviation.

Wear and Scratch. Dry sliding and reciprocating wear tests were carried out in an RTEC universal reciprocating tribometer using 6 mm-diameter AISI 52100 balls as the counterface. Tests were carried out under a normal load of 5 N and at a frequency of 10 Hz for a total time of 60 min. The stroke length was 3.5 mm, corresponding to 126 m of sliding distance. Wear volume loss (mm³) was measured using Gwyddion software and converted to wear rates (mm³/N·m). Unidirectional scratch tests were performed using a Rockwell diamond stylus with a radius of 200  $\mu$ m and a tip angle of 120°. Tests were carried out under progressive increasing load in the range of 5–180 N with 10 mm length. The loading rate and lateral displacement speed were selected as 100 N/min and 6 mm/min, respectively.

MD Simulation. MD simulation was performed using a large-scale atomic/molecular massively parallel simulator (LAMMPS) using EAM potential for Ni-P metallic glass. 61 Three models containing ~88,000 atoms with different compositions were generated and melted at 2000 K. The alloys were maintained at a high temperature for 1 (ns) followed by quenching at a rate of  $10^{13}\ (\text{K/s})$  to obtain an amorphous structure in the case of  $Ni_{90}P_{10}$  and  $Ni_{85}P_{15}$  alloys. All the thermodynamic processes were carried out with the NPT (constant number of particles, pressure, and temperature) ensemble based on the Nose-Hoover thermostat and barostat with a time step of 1 (fs) and periodic boundary conditions in three dimensions. For postprocessing of MD simulation, OVITO was employed as a visualization tool to perform Voronoi analysis to identify and quantify the types and numbers of polyhedra. Compression tests were carried out for the amorphous alloys with dimensions of 8.5 nm  $(X) \times$  8.5 nm  $(Y) \times 42.5$  nm (Z) at a constant strain rate of  $10^9$  s<sup>-1</sup>. Engineering stress-strain curves were plotted, and yield strength was measured at 0.2% offset.

## CONCLUSIONS

 $Ni_{100-x}P_x$  (x = 0, 5, 10, 15, 25 at. %) alloys were synthesized across multiple length scales using the facile and easily scalable

pulsed electrodeposition approach. Amorphous alloys were obtained for phosphorus content in the range of 10-15 at. % with glass transition temperature in the range of 310-315 °C and crystallization temperature in the range of 340-350 °C. The Ni<sub>00</sub>P<sub>10</sub> alloy showed higher strain rate sensitivity, smooth nanoindentation load-depth curve, and multiple shear band formations in micropillar compression, all of which indicate more homogeneous flow and greater plasticity compared to Ni<sub>85</sub>P<sub>15</sub>. Higher hardness, yield strength, and strain localization for the Ni<sub>85</sub>P<sub>15</sub> alloy were attributed to its local short-range atomic order. Bicapped square antiprism polyhedra clusters were connected through two-atom connection in Ni<sub>90</sub>P<sub>10</sub>, leading to more homogeneous plastic flow, whereas relatively higher fraction of three-atom connection resulted in localized deformation for Ni<sub>85</sub>P<sub>15</sub>. The ductile behavior of Ni<sub>90</sub>P<sub>10</sub> compared to Ni<sub>85</sub>P<sub>15</sub> was further confirmed in progressive scratch tests, where a series of nested microcracks were observed for Ni<sub>90</sub>P<sub>10</sub>, while extensive cracking that propagated outside the grooves was observed for Ni<sub>85</sub>P<sub>15</sub>. This demonstrates the versatility of electrodeposition as an effective toolbox for tuning the properties of metallic glasses by a slight change in alloy chemistry, which is a major hindrance in the currently used melt quenching approach.

## ASSOCIATED CONTENT

## **5** Supporting Information

The Supporting Information is available free of charge at https://pubs.acs.org/doi/10.1021/acsami.0c22153.

Electrodeposited alloys in a wide range of compositions; electrodeposited Ni–P coatings in complex geometries; mechanical behavior of the Ni–P alloy electrodeposited on copper wire; microstructure dependence on current density of electrodeposition; and yield strength of Ni $_{85}$ P $_{15}$  and Ni $_{90}$ P $_{10}$  alloys obtained from MD simulation (PDF)

 $Ni_{90}P_{10}$  micropillar compression video (MP4)  $Ni_{85}P_{15}$  micropillar compression video (MP4)

# AUTHOR INFORMATION

### **Corresponding Author**

Sundeep Mukherjee — Department of Materials Science and Engineering, University of North Texas, Denton, Texas 76203, United States; orcid.org/0000-0002-1954-0045; Phone: 940-565-4170; Email: sundeep.mukherjee@unt.edu; Fax: 940-565-2944

### **Authors**

Maryam Sadeghilaridjani – Department of Materials Science and Engineering, University of North Texas, Denton, Texas 76203, United States

Yu Chia Yang – Department of Materials Science and Engineering, University of North Texas, Denton, Texas 76203, United States

Vahid Hasannaeimi – Department of Materials Science and Engineering, University of North Texas, Denton, Texas 76203, United States

Chaitanya Mahajan — Department of Materials Science and Engineering, University of North Texas, Denton, Texas 76203, United States; orcid.org/0000-0002-9490-2181

Shristy Jha – Department of Materials Science and Engineering, University of North Texas, Denton, Texas 76203, United States Mayur Pole – Department of Materials Science and Engineering, University of North Texas, Denton, Texas 76203, United States

Zhenhai Xia — Department of Materials Science and Engineering, University of North Texas, Denton, Texas 76203, United States; Occid.org/0000-0002-0881-2906

Complete contact information is available at: https://pubs.acs.org/10.1021/acsami.0c22153

## **Author Contributions**

M.S. conducted nanoindentation experiments and wrote the paper, Y.C.Y. and Z.X. performed the MD simulation, V.H. and C.M. contributed to the multiscale manufacturing process, S.J. conducted micropillar compression tests, M.P. conducted tribology experiments, and S.M. supervised the work and contributed to the revision of the manuscript.

### **Funding**

This work was supported by funding from the National Science Foundation (NSF) under grant numbers 1561886, 1919220, and 1762545. Any opinions, findings, and conclusions expressed in this paper are those of the authors and do not necessarily reflect the views of the National Science Foundation (NSF).

#### Notes

The authors declare no competing financial interest.

## REFERENCES

- (1) Klement, W.; Willens, R. H.; Duwez, P. Non-crystalline Structure in Solidified Gold-Silicon Alloys. *Nature* **1960**, *187*, 869–870.
- (2) Inoue, A. Stabilization of Metallic Supercooled Liquid and Bulk Amorphous Alloys. *Acta Mater.* **2000**, *48*, 279–306.
- (3) Telford, M. The Case for Bulk Metallic Glass. *Mater. Today* **2004**, 7, 36-43.
- (4) Schroers, J. Processing of Bulk Metallic Glass. Adv. Mater. 2010, 22, 1566–1597.
- (5) Hasannaeimi, V.; Mukherjee, S. Highly Catalytic Amorphous Ni-P Synthesized via Pulsed Electrodeposition. *Adv. Eng. Mater.* **2019**, *21*, 1801122.
- (6) Sun, C.; Li, J.; Shuang, S.; Zeng, H.; Luo, J.-L. Effect of Defect on Corrosion Behavior of Electroless Ni-P Coating in CO2-Saturated NaCl Solution. *Corros. Sci.* **2018**, *134*, 23–37.
- (7) Jeong, D. H.; Erb, U.; Aust, K. T.; Palumbo, G. The relationship between hardness and abrasive wear resistance of electrodeposited nanocrystalline Ni-P coatings. *Scr. Mater.* **2003**, *48*, 1067–1072.
- (8) Lelevic, A.; Walsh, F. C. Electrodeposition of Ni P alloy coatings: A review. Surf. Coat. Technol. 2019, 369, 198–220.
- (9) Shao, L.; Ketkaew, J.; Gong, P.; Zhao, S.; Sohn, S.; Bordeenithikasem, P.; Datye, A.; Mota, R. M. O.; Liu, N.; Kube, S. A.; Liu, Y.; Chen, W.; Yao, K.; Wu, S.; Schroers, J. Effect of Chemical Composition on the Fracture Toughness of Bulk Metallic Glasses. *Materialia* 2020, 12, 100828.
- (10) Jafary-Zadeh, M.; Tavakoli, R.; Koh, J. J.; Aitken, Z. H.; Zhang, Y.-W. Effect of Chemical Composition and Affinity on the Short- and Medium-Range Order Structures and Mechanical Properties of Zr-Ni-Al Metallic Glass. *J. Non-Cryst. Solids* **2017**, *456*, 68–75.
- (11) Gross, O.; Neuber, N.; Kuball, A.; Bochtler, B.; Hechler, S.; Frey, M.; Busch, R. Signatures of Structural Differences in Pt-P- and Pd-P-Based Bulk Glass-Forming Liquids. *Commun. Phys.* **2019**, *2*, 83.
- (12) Sridharan, K.; Sheppard, K. Electrochemical Characterization of Fe-Ni-P Alloy Electrodeposition. *J. Appl. Electrochem.* **1997**, *27*, 1198–1206.
- (13) Hasannaeimi, V.; Wang, X.; Salloom, R.; Xia, Z.; Schroers, J.; Mukherjee, S. Nanomanufacturing of Non-Noble Amorphous Alloys

- for Electrocatalysis. ACS Appl. Energy Mater. 2020, 3 (12), 12099-12107.
- (14) Kim, T.-Y.; Son, H.-J.; Lim, S.-K.; Song, Y.; Park, H.-S.; Suh, S.-J. Electroless Nickel Alloy Deposition on SiO2 for Application as a Diffusion Barrier and Seed Layer in 3D Copper Interconnect Technology. *J. Nanosci. Nanotechnol.* **2014**, *14*, 9515.
- (15) Mohri, M.; Wang, D.; Ivanisenko, J.; Gleiter, H.; Hahn, H. Thermal Stability of the Ti-Zr-Cu-Pd Nano-Glassy Thin Films. *J. Alloys Compd.* **2018**, 735, 2197–2204.
- (16) Younes, O.; Zhu, L.; Rosenberg, Y.; Shacham-Diamand, Y.; Gileadi, E. Electroplating of Amorphous Thin Films of Tungsten/Nickel Alloys. *Langmuir* **2001**, *17*, 8270–8275.
- (17) Wang, J. G.; Choi, B. W.; Nieh, T. G.; Liu, C. T. Crystallization and nanoindentation behavior of a bulk Zr-Al-Ti-Cu-Ni amorphous alloy. *J. Mater. Res.* **2000**, *15*, 798–807.
- (18) Burgess, T.; Ferry, M. Nanoindentation of Metallic Glasses. *Mater. Today* **2009**, 12, 24–32.
- (19) Shi, Y.; Falk, M. L. Stress-Induced Structural Transformation and Shear Banding During Simulated Nanoindentation of a Metallic Glass. *Acta Mater.* **2007**, *55*, 4317–4324.
- (20) Schuh, C. A.; Nieh, T. G. A Nanoindentation Study of Serrated Flow in Bulk Metallic Glasses. *Acta Mater.* **2003**, *51*, 87–99.
- (21) Greer, A. L.; Cheng, Y. Q.; Ma, E. Shear Bands in Metallic Glasses. *Mater. Sci. Eng.*, R **2013**, 74, 71–132.
- (22) Schuh, C. A.; Lund, A. C.; Nieh, T. G. New Regime of Homogeneous Flow in the Deformation Map of Metallic Glasses: Elevated Temperature Nanoindentation Experiments and Mechanistic Modeling. *Acta Mater.* **2004**, *52*, 5879–5891.
- (23) Sadeghilaridjani, M.; Muskeri, S.; Hasannaeimi, V.; Pole, M.; Mukherjee, S. Strain Rate Sensitivity of a Novel Refractory High Entropy Alloy: Intrinsic Versus Extrinsic Effects. *Mater. Sci. Eng., A* **2019**, 766, 138326.
- (24) Torre, F. H. D.; Dubach, A.; Siegrist, M. E.; Löffler, J. F. Negative Strain Rate Sensitivity in Bulk Metallic Glass and Its Similarities with the Dynamic Strain Aging Effect During Deformation. *Appl. Phys. Lett.* **2006**, *89*, 091918.
- (25) Spaepen, F. A Microscopic Mechanism for Steady State Inhomogeneous Flow in Metallic Glasses. *Acta Metall.* **1977**, 25, 407–415.
- (26) Pan, D.; Inoue, A.; Sakurai, T.; Chen, M. W. Experimental Characterization of Shear Transformation Zones for Plastic Flow of Bulk Metallic Glasses. *PNAS* **2008**, *105*, 14769–14772.
- (27) Kim, S. Y.; Oh, H. S.; Park, E. S. A hidden variable in shear transformation zone volume versus Poisson's ratio relation in metallic glasses. *APL Mater.* **2017**, *5*, 106105.
- (28) Liu, S. T.; Wang, Z.; Peng, H. L.; Yu, H. B.; Wang, W. H. The Activation Energy and Volume of Flow Units of Metallic Glasses. *Scr. Mater.* **2012**, *67*, 9–12.
- (29) Wang, W. H.; Dong, C.; Shek, C. H. Bulk Metallic Glasses. *Mater. Sci. Eng., R* **2004**, *44*, 45–89.
- (30) Wang, W. H. Correlations between elastic moduli and properties in bulk metallic glasses. J. Appl. Phys. 2006, 99, 093506.
- (31) Bian, Z.; Wang, R. J.; Zhao, D. Q.; Pan, M. X.; Wang, Z. X.; Wang, W. H. Excellent ultrasonic absorption ability of carbon-nanotube-reinforced bulk metallic glass composites. *Appl. Phys. Lett.* **2003**, *82*, 2790–2792.
- (32) Johnson, W. L. Bulk Amorphous Metal-an Emerging Engineering Material. *JOM* **2002**, *54*, 40–43.
- (33) Xu, D.; Duan, G.; Johnson, W. L.; Garland, C. Formation and Properties of New Ni-Based Amorphous Alloys with Critical Casting Thickness Up to 5 mm. *Acta Mater.* **2004**, *52*, 3493–3497.
- (34) Inoue, A.; Shen, B. L.; Chang, C. T. Super-high strength of over 4000 MPa for Fe-based bulk glassy alloys in [(Fe1-xCox)-0.75B0.2Si0.05]96Nb4 system. *Acta Mater.* **2004**, *52*, 4093–4099.
- (35) Lambson, E. F.; Lambson, W. A.; Macdonald, J. E.; Gibbs, M. R. J.; Saunders, G. A.; Turnbull, D. Elastic behavior and vibrational anharmonicity of a bulkPd40Ni40P20metallic glass. *Phys. Rev. B: Condens. Matter Mater. Phys.* 1986, 33, 2380–2385.

- (36) Chen, H. S. Alloying Effect on the Viscous Flow in Metallic Glasses. *J. Non-Cryst. Solids* **1978**, 29, 223–229.
- (37) Chen, H. S.; Turnbull, D. Thermal Evidence of a Glass Transition in Gold-silicon-germanium Alloy. *Appl. Phys. Lett.* **1967**, 10, 284–286.
- (38) Narayan, R. L.; Boopathy, K.; Sen, I.; Hofmann, D. C.; Ramamurty, U. On the Hardness and Elastic Modulus of Bulk Metallic Glass Matrix Composites. *Scr. Mater.* **2010**, *63*, 768–771.
- (39) Keryvin, V.; Hoang, V. H.; Shen, J. Hardness, Toughness, Brittleness and Cracking Systems in an Iron-Based Bulk Metallic Glass by Indentation. *Intermetallics* **2009**, *17*, 211–217.
- (40) Zhang, Y.; Zhao, D. Q.; Pan, M. X.; Wang, W. H. Glass Forming Properties of Zr-Based Bulk Metallic Alloys. *J. Non-cryst. Solids* **2003**, *315*, 206–210.
- (41) Cheung, T. L.; Shek, C. H. Thermal and mechanical properties of Cu-Zr-Al bulk metallic glasses. *J. Alloys Compd.* **200**7, 434–435, 71–74
- (42) Gu, J.; Song, M.; Ni, S.; Guo, S.; He, Y. Effects of annealing on the hardness and elastic modulus of a Cu36Zr48Al8Ag8 bulk metallic glass. *Mater. Des.* **2013**, *47*, 706–710.
- (43) Ponnambalam, V.; Poon, S. J.; Shiflet, G. J. Fe-Based Bulk Metallic Glasses with Diameter Thickness Larger than One Centimeter. J. Mater. Res. 2004, 19, 1320–1323.
- (44) Zhang, H. W.; Subhash, G.; Jing, X. N.; Kecskes, L. J.; Dowding, R. J. Evaluation of hardness-yield strength relationships for bulk metallic glasses. *Philos. Mag. Lett.* **2006**, *86*, 333–345.
- (45) Pan, X. F.; Zhang, H.; Zhang, Z. F.; Stoica, M.; He, G.; Eckert, J. Vickers Hardness and Compressive Properties of Bulk Metallic Glasses and Nanostructure-Dendrite Composites. *J. Mater. Res.* **2005**, 20, 2632–2638.
- (46) Wang, J.; Li, R.; Hua, N.; Zhang, T. Co-Based Ternary Bulk Metallic Glasses with Ultrahigh Strength and Plasticity. *J. Mater. Res.* **2011**, *26*, 2072–2079.
- (47) Kong, J.; Xiong, D.; Li, J.; Yuan, Q.; Tyagi, R. Effect of Flash Temperature on Tribological Properties of Bulk Metallic Glasses. *Tribol. Lett.* **2009**, *35*, 151–158.
- (48) Huang, Y.; Fan, H.; Wang, D.; Sun, Y.; Liu, F.; Shen, J.; Sun, J.; Mi, J. The Effect of Cooling Rate on the Wear Performance of a ZrCuAlAg Bulk Metallic Glass. *Mater. Des.* **2014**, *58*, 284–289.
- (49) Liu, L.; Qiu, C. L.; Huang, C. Y.; Yu, Y.; Huang, H.; Zhang, S. M. Biocompatibility of Ni-Free Zr-Based Bulk Metallic Glasses. *Intermetallics* **2009**, *17*, 235–240.
- (50) Zhang, G. Q.; Li, X. J.; Shao, M.; Wang, L. N.; Yang, J. L.; Gao, L. P.; Chen, L. Y.; Liu, C. X. Wear Behavior of a Series of Zr-Based Bulk Metallic Glasses. *Mater. Sci. Eng., A* **2008**, 475, 124–127.
- (51) Liao, Z.; Hua, N.; Chen, W.; Huang, Y.; Zhang, T. Correlations Between the Wear Resistance and Properties of Bulk Metallic Glasses. *Intermetallics* **2018**, *93*, 290–298.
- (52) Fleury, E.; Lee, S. M.; Ahn, H. S.; Kim, W. T.; Kim, D. H. Tribological Properties of Bulk Metallic Glasses. *Mater. Sci. Eng., A* **2004**, *375*–*377*, *276*–*279*.
- (53) Rahaman, M. L.; Zhang, L.; Liu, M.; Liu, W. Surface Roughness Effect on the Friction and Wear of Bulk Metallic Glasses. *Wear* **2015**, 332–333, 1231–1237.
- (54) Maddala, D. R.; Mubarok, A.; Hebert, R. J. Sliding wear behavior of Cu50Hf41.5Al8.5 bulk metallic glass. *Wear* **2010**, 269, 572–580.
- (55) Maddala, D. R.; Hebert, R. J. Sliding wear behavior of Fe50–xCr15Mo14C15B6Erx (x=0, 1, 2at%) bulk metallic glass. *Wear* **2012**, 294–295, 246–256.
- (56) Sarkar, A. D. Friction and Wear; Academic Press: London, 1980; pp 205-209.
- (57) Zhu, F.; Song, S.; Reddy, K. M.; Hirata, A.; Chen, M. Spatial Heterogeneity as the Structure Feature for Structure–Property Relationship of Metallic Glasses. *Nat. Commun.* **2018**, *9*, 3965.
- (58) Cheng, Y. Q.; Ma, E. Atomic-level structure and structure-property relationship in metallic glasses. *Prog. Mater. Sci.* **2011**, *56*, 379–473.

- (59) Liu, X. J.; Xu, Y.; Lu, Z. P.; Hui, X.; Chen, G. L.; Zheng, G. P.; Liu, C. T. Atomic Packing Symmetry in the Metallic Liquid and Glass States. *Acta Mater.* **2011**, *59*, 6480–6488.
- (60) Wu, Z. W.; Li, M. Z.; Wang, W. H.; Liu, K. X. Hidden Topological Order and Its Correlation with Glass-Forming Ability in Metallic Glasses. *Nat. Commun.* **2015**, *6*, 6035.
- (61) Sheng, H. W.; Ma, E.; Kramer, M. J. Relating Dynamic Properties to Atomic Structure in Metallic Glasses. *JOM* **2012**, *64*, 856–881.
- (62) Liu, X. J.; Xu, Y.; Hui, X.; Lu, Z. P.; Li, F.; Chen, G. L.; Lu, J.; Liu, C. T. Metallic Liquids and Glasses: Atomic Order and Global Packing. *Phys. Rev. Lett.* **2010**, *105*, 155501.
- (63) Fang, X. W.; Wang, C. Z.; Hao, S. G.; Kramer, M. J.; Yao, Y. X.; Mendelev, M. I.; Ding, Z. J.; Napolitano, R. E.; Ho, K. M. Spatially Resolved Distribution Function and the Medium-Range Order in Metallic Liquid and Glass. *Sci. Rep.* **2011**, *1*, 194.
- (64) Pan, S. P.; Qin, J. Y.; Wang, W. M.; Gu, T. K. Origin of Splitting of the Second Peak in the Pair-Distribution Function for Metallic Glasses. *Phys. Rev. B: Condens. Matter Mater. Phys.* **2011**, 84, 092201.
- (65) Ding, J.; Ma, E.; Asta, M.; Ritchie, R. O. Second-Nearest-Neighbor Correlations from Connection of Atomic Packing Motifs in Metallic Glasses and Liquids. *Sci. Rep.* **2015**, *5*, 17429.
- (66) Ma, D.; Stoica, A. D.; Wang, X.-L. Power-Law Scaling and Fractal Nature of Medium-Range Order in Metallic Glasses. *Nat. Mater.* **2009**, *8*, 30–34.
- (67) Sheng, H. W.; Luo, W. K.; Alamgir, F. M.; Bai, J. M.; Ma, E. Atomic packing and short-to-medium-range order in metallic glasses. *Nature* **2006**, 439, 419–425.
- (68) Hirata, A.; Guan, P.; Fujita, T.; Hirotsu, Y.; Inoue, A.; Yavari, A. R.; Sakurai, T.; Chen, M. Direct Observation of Local Atomic Order in a Metallic Glass. *Nat. Mater.* **2011**, *10*, 28–33.
- (69) Wang, N.; Ding, J.; Yan, F.; Asta, M.; Ritchie, R. O.; Li, L. Spatial Correlation of Elastic Heterogeneity Tunes the Deformation Behavior of Metallic Glasses. *npj Comput. Mater.* **2018**, *4*, 19.
- (70) Oliver, W. C.; Pharr, G. M. Measurement of Hardness and Elastic Modulus by Instrumented Indentation: Advances in Understanding and Refinements to Methodology. *J. Mater. Res.* **2004**, *19*, 3–20.